# 3

# The unbounded gradient model

A fundamental problem in double-diffusive convection concerns the equilibrium transport of temperature, salinity, chemical tracers and momentum. The quantification of double-diffusive fluxes and their dependencies is an essential step in linking the microstructure dynamics with larger scales of motion − a problem that has motivated numerous laboratory and field experiments, as well as theoretical and numerical models. Linear stability theory for double-diffusion (Chapter 2) is well developed and fully understood. However, it does not explain the equilibration mechanisms, or predict the saturation amplitude, of the unstable perturbations. The problem of equilibration is complicated and principally nonlinear. Only recently have we started to see the first signs of a consensus between theorists, modelers and observationalists with regard to the typical magnitudes of double-diffusive transport of heat and salt in the ocean and its variation with environmental parameters. Our discussion of nonlinear effects starts with the unbounded gradient system, which is used to explain the dynamics of double-diffusive mixing in smooth background temperature and salinity gradients. We focus on theoretical models, which attempt to predict the equilibrium transport from first principles. However, their success is judged in terms of consistency with observations and simulations.

## 3.1 Flux-gradient laws

The unbounded gradient models are based on an assumption that, in relatively smooth background gradients of temperature and salinity, the intensity of double-diffusive convection is controlled by the local $T$–$S$ gradients and, to a lesser extent, by the background shear. The separation from physical boundaries and the scales of inhomogeneity of the background flow are assumed to be too large to affect local properties of double-diffusive convection. This assumption may not apply for diffusive layering, which is better represented by interfacial models (Chapter 4). Therefore, the vast majority of unbounded models are focused on the

32

salt-finger case and we shall follow suit. As with any idealization, the unbounded fingering model should be applied to observations and laboratory experiments with caution. Examples can be constructed in which the intensity of salt fingers is not uniquely determined by the background gradients but affected by such parameters as the vertical extent of the double-diffusive region (e.g., Radko and Stern, 2000). However, such counter-examples are rather rare and somewhat artificial. What makes the unbounded model of salt fingers particularly robust and relevant in the oceanographic context is a clear scale separation that generally exists between salt fingers and larger features of circulation.

The ultimate goal of the unbounded model is to formulate explicit relationships between the vertical eddy transport of temperature and salinity and their local gradients:

$$
\begin{cases}
\overline{w'_{\text{dim}} T'}_{\text{dim}} = F_{T\,\text{dim}} \left( \dfrac{\partial \bar{T}}{\partial z}, \dfrac{\partial \bar{S}}{\partial z}, k_T, k_S, v \right), \\[3mm]
\overline{w'_{\text{dim}} S'}_{\text{dim}} = F_{S\,\text{dim}} \left( \dfrac{\partial \bar{T}}{\partial z}, \dfrac{\partial \bar{S}}{\partial z}, k_T, k_S, v \right),
\end{cases}
\tag{3.1}
$$

were $(\overline{w'_{\text{dim}} T'_{\text{dim}}}, \overline{w'_{\text{dim}} S'_{\text{dim}}})$ are the dimensional eddy-induced fluxes. The problem can be simplified based on dimensional reasoning: any dimensionless number can only be determined by the other dimensionless parameters. As discussed in Chapter 1, the key dimensionless governing parameters in the unbounded model are limited to the density ratio ($R_\rho$), diffusivity ratio ($\tau$) and Prandtl number ($Pr$). Following the analogy with thermal convection, the intensity of double-diffusive mixing is commonly quantified by the Nusselt number, defined as the ratio of the eddy-induced and conductive heat fluxes:

$$
Nu = \frac{-\overline{w'_{\text{dim}} T'_{\text{dim}}}}{k_T \frac{\partial \bar{T}}{\partial z}} = Nu(R_\rho, \tau, Pr).
\tag{3.2}
$$

The same non-dimensional parameters control another key measure of vertical transport, the flux ratio (Chapter 2):

$$
\gamma = \frac{\alpha \overline{w'_{\text{dim}} T'_{\text{dim}}}}{\beta \overline{w'_{\text{dim}} S'_{\text{dim}}}} = \gamma \left( R_\rho, \tau, Pr \right).
\tag{3.3}
$$

While the estimate of the flux ratio (3.3) can be made on the basis of linear theory, prediction of the $Nu(R_\rho)$ dependence − the core problem of double-diffusive convection − is impossible without taking nonlinearity into account. An alternative form for the flux-gradient laws (3.2) and (3.3) can be given in terms of the eddy

diffusivities of heat and salt ($K_T$, $K_S$):

$$\begin{cases} K_T = -\dfrac{\overline{w'_{\dim} T'_{\dim}}}{\bar{T}_z} = k_T Nu, \\[2ex] K_S = -\dfrac{\overline{w'_{\dim} S'_{\dim}}}{\bar{S}_z} = K_T \dfrac{R_\rho}{\gamma} = \dfrac{k_T R_\rho}{\gamma} Nu. \end{cases} \tag{3.4}$$

Thus, for any given fluid, the eddy diffusivities in the unbounded gradient model are determined entirely by the density ratio.

Double-diffusive convection theory places much lesser emphasis on large-scale momentum transfer than on *T–S* transfer. Numerical simulations indicate that, unlike diffusivity, the eddy viscosity of salt fingers is actually less than its molecular counterpart (Stern *et al.*, 2001). Thus, even neglecting eddy viscosity completely may have relatively minor ramifications for the large-scale dynamics. This suggestion, however, has been confirmed only in the oceanographic heat–salt context. Limited evidence suggests that the eddy viscosity due to double-diffusion may be essential (Radko, 2010) for the dynamics of low Prandtl number fluids, such as occur in astrophysical systems (Chapter 12).

## 3.2 Secondary instabilities: Stern–Kunze constraint and Holyer modes

Numerous attempts have been made to deduce flux-gradient laws from first principles. The first and, perhaps, the most influential idea was presented by Stern (1969), who suggested that the linear growth of salt fingers is arrested when the Stern number

$$A = \frac{F_{\rho\,\dim}}{\nu \bar{\rho}_z}, \tag{3.5}$$

where $F_{\rho\,\dim}$ is the vertical density flux, reaches O(1). Stern's physical argument is compelling. When $A$ exceeds unity, the unbounded salt-finger system becomes unstable with respect to the so-called collective instability, the term referring to the spontaneous excitation of gravity waves by salt fingers. Stern suggested that collective instability − to be considered in greater detail in Chapter 6 − could disrupt salt fingers, thereby arresting amplification of primary growing modes.

At first glance, various pieces of indirect evidence seem to validate Stern's hypothesis. Oceanographic measurements (Hebert, 1988; Inoue *et al.*, 2008) indeed suggest the order one values of $A$. Kunze (1987) gave an alternative argument in support of the Stern number constraint. He speculated that the well-known Richardson number criterion for dynamic instability of horizontal inviscid parallel flows (Richardson, 1920; Howard, 1961; Miles, 1961) can be extended to salt fingers. The Richardson number is defined as the ratio of the squared buoyancy

frequency and the squared velocity shear. For instability to occur, it is required to be less than 1/4. Kunze showed that the Richardson number of 1/4 based on the salt-finger scales is equivalent to the Stern number of unity. His model further assumes that the growth of salt fingers is arrested when they become susceptible to their secondary dynamic instabilities and therefore $A \sim 1$ sets the equilibrium condition.

However, despite the very promising start, the theory of finger equilibration evolved into one of the most controversial topics in double-diffusive convection. The first seeds of doubt as to the relevance of the $A$-based theory were planted when laboratory experimentalists started to use sugar and salt as diffusive substances. Such experiments became particularly popular for practical reasons. In heat–salt experiments it is difficult to avoid − or accurately take into account − the heat loss across the walls of the tank. The parameters in sugar–salt experiments ($\tau \approx 1/3$, $Pr \approx 10^3$) differ from the oceanographically relevant heat–salt case ($\tau \approx 0.01$, $Pr \approx 7$) but the dynamics appear to be similar. The first experiment of this nature was performed by Stern and Turner (1969) and was followed by numerous studies offering more detailed and precise measurements. Stern numbers realized in sugar–salt experiments are extremely low. Lambert and Demenkow (1972) reported values as small as $A = 2 \cdot 10^{-3}$, Griffiths and Ruddick (1980) and Krishnamurti (2003) found that, typically, $A \sim 0.1$–$0.01$, bringing into question the generality of Stern's constraint.

On the theoretical side, a critical advance was made by Holyer (1984), who performed a formal linear stability analysis for the vertical steady salt fingers. She discovered the direct, relatively small-scale − comparable to the salt-finger width − secondary instabilities, which typically grow much faster than the collective instability modes. Furthermore, unlike collective instabilities, Holyer modes grow regardless of the (finite) amplitude of salt fingers. A corollary of these findings is that salt fingers are more likely to be disrupted by the Holyer mechanism, rather than by collective instabilities. The schematic in Figure 3.1 illustrates the action of secondary instabilities, distorting the vertical fingers and ultimately arresting their growth.

Numerical simulations have shed extra light on the mechanics of equilibration. Two-dimensional experiments in Whitfield *et al.* (1989) performed with various molecular parameters ($Pr$, $\tau$) resulted in Stern numbers that varied by a factor of 3400. A series of simulations by Shen (1993) in which the density ratio was systematically varied whereas ($Pr$, $\tau$) were kept constant revealed that the Stern number ($A$) is rapidly decreasing with $R_\rho$. This finding was confirmed by recent three-dimensional simulations in Traxler *et al.* (2011a), who showed that the Stern number decreases by two orders of magnitude from $R_\rho = 1.2$ to $R_\rho = 10$. Diagnostics of the numerical simulations in Radko and Stern (1999) revealed that the
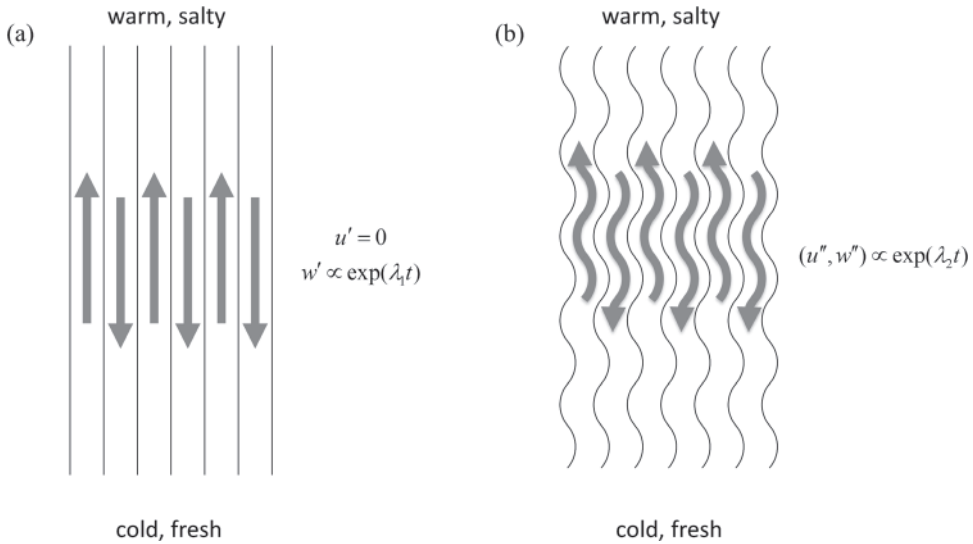
Figure 3.1 Schematic diagram illustrating development of primary salt-finger instabilities in the form of vertical elevator modes (a) and their ultimate equilibration by secondary instabilities (b) acting to distort fingers, thereby reducing the vertical transport of heat and salt. From Schmitt (2012).

equilibration occurs by means of the nonlinear interaction of primary instabilities with Holyer modes. The equilibrium heat and salt fluxes recorded in simulations (e.g., Stern *et al.*, 2001; Traxler *et al.*, 2011a) and even diagnosed from oceanic field measurements (St. Laurent and Schmitt, 1999) monotonically decrease with the density ratio, whereas the opposite trend is expected based on the Stern–Kunze constraint. In view of all the numerical, laboratory and observational evidence, it is tempting to conclude that the order-one values of *A* frequently observed in the ocean are a peculiar coincidence.

It should be emphasized at this point that, while numerical studies contest the Stern–Kunze constraint for the equilibrium amplitude of salt fingers, the collective instability itself is revealed very clearly in simulations (Stern *et al.*, 2001; Stern and Simeonov, 2002; Stellmach *et al.*, 2011). Likewise, there is no reason to doubt that the intensity of collective instability is controlled by the Stern number. What *is* highly questionable is the link between the Stern number and the amplitude saturation of salt fingers, which can grow even in the presence of very active collective instabilities. Concerns with regard to the Stern–Kunze constraint motivate development of alternative models of equilibration. While a comprehensive nonlinear theory of salt fingers is still lacking, double-diffusers have started to fill some gaps in the understanding of equilibration and have already successfully treated various limits. Some promising results in this direction are summarized next.

## 3.3  Weakly nonlinear models

Traditionally, saturation mechanisms for various instabilities of fluids are identified and explained by developing weakly nonlinear asymptotic models. Specific examples are discussed and summarized in numerous textbooks (e.g., Drazin and Reid, 1981; Godreche and Manneville, 2005) and the procedure is briefly outlined below. Inspired and guided by the treatment of Rayleigh–Bénard convection (Malkus and Veronis, 1958), weakly nonlinear models focus on the marginally unstable regime. The governing equations are expanded in a small parameter measuring the strength of the instability. This quantity, denoted by $\varepsilon$ hereafter, is usually defined as the difference in one of the key parameters between the current configuration and the one with zero growth rate. After collecting terms of the same order in $\varepsilon$, one is left with a hierarchy of simpler, analytically solvable problems. It is often possible, by sequentially solving these balanced equations, to relate the amplitude of instability to $\varepsilon$ and thus to the governing parameters. Another precious product of weakly nonlinear models is related to the insight they bring into the dynamics of equilibration. Complexities of the original governing equations usually preclude the direct association of individual terms with distinct mechanisms. In contrast, each balance in the weakly nonlinear models usually offers straightforward physical interpretation, making it possible to trace the chain of events leading to equilibration. The price paid for tractability is the limited accuracy outside of the weakly unstable range and, for most intents and purposes, it is a fair price.

The weakly nonlinear models for salt fingers have been explored in several studies (Proctor and Holyer, 1986; Stern and Radko, 1998; Radko and Stern, 1999, 2000; Stern and Simeonov, 2004; Radko, 2010). In the unbounded model, the key parameter is the density ratio and the marginally unstable point (Chapter 2) corresponds to $R_\rho = \tau^{-1}$. Thus, a sensible choice for the expansion parameter in the weakly nonlinear model could be

$$\varepsilon = R_\rho^{-1} - \tau. \tag{3.6}$$

The limit $\varepsilon \to 0$ has been explored most recently by Radko (2010). The resulting weakly nonlinear theory predicted that (i) the equilibrium fluxes of heat and salt are proportional to $\varepsilon^2$ and (ii) the equilibration occurs through the interaction of salt fingers with Holyer (1984) instabilities. More specifically, theory attributes the equilibration of salt fingers to a combination of two processes: the triad interaction and spontaneous development of the mean vertical shear. The non-resonant triad interactions control the equilibration of linear growth for moderate and large values of Prandtl number (*Pr*) and for slightly unstable parameters. For small *Pr* and/or rigorous instabilities, the mean shear effects become essential. These theoretical predictions are consistent with the two-dimensional direct numerical simulations
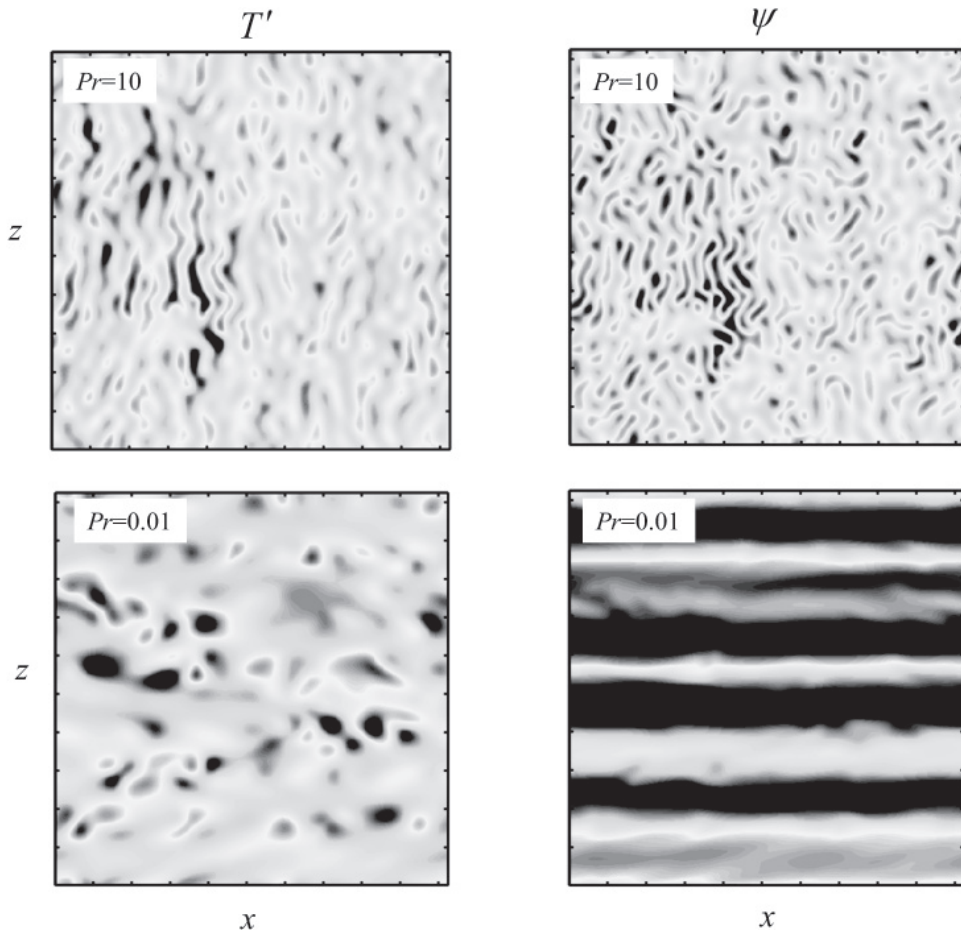
Figure 3.2 Variability of the salt-finger patterns. Instantaneous temperature (left) and streamfunction (right) fields from direct numerical simulations (DNS) are presented for $Pr = 10$ (top) and for $Pr = 0.01$ (bottom). In all cases $R_\rho = 2.8$ and $t = 1/3$. Red color corresponds to high values and low values are shown in blue. From Radko (2010). See color plates section.

(DNS) shown in Figure 3.2. For $Pr = 10$ (Fig. 3.2, top) salt fingers appear in the form of narrow vertically oriented filaments. The pattern changes dramatically for smaller $Pr = 0.01$ (Fig. 3.2, bottom). The temperature field is now dominated by disorganized eddies with comparable vertical and horizontal dimensions. The streamfunction $\psi$, defined by $(u, w) = (-\psi_z, \psi_x)$, assembles into well-defined horizontal bands, representing a vigorous parallel shear flow.

Insightful as they might be, weakly nonlinear models offer a mostly qualitative description of heat–salt fingering. Salt fingers in the ocean are strongly nonlinear. Much of the mid-latitude thermocline is characterized by $1 < R_\rho < 3$, a small

fraction of the net salt-finger favorable range $1 < R_\rho < \tau^{-1} \approx 100$. Typical oceanic parameters are greatly separated from the marginal instability point ($R_\rho = \tau^{-1}$), being in fact closer to the opposite end of the salt-finger range, the boundary between salt fingers and static instability ($R_\rho = 1$). Unfortunately, the general analytical theory for strongly nonlinear instabilities is virtually non-existent. Users have to develop tractable approximations on a case-by-case basis. The next section summarizes several representative attempts to conceptualize fully nonlinear processes in double-diffusive convection. Understandably, the following theories may not be as rigorous, conventional, physical, transparent, or even elegant as their weakly nonlinear counterparts. The development of strongly nonlinear models is motivated by only one consideration – their relevance.

## 3.4 Phenomenological and empirical models

Ironically, it was perhaps the profound influence of the collective instability theory (Stern, 1969) on double-diffusive research in the 1970s and 80s that led to the relatively slow development of the fully nonlinear equilibrium theory for salt fingers. New models, and even the realization that new models are needed, did not come about until gradually accumulating evidence gave a reason to question the early views. A few equilibrium models – the viable alternatives to the collective instability theory – are summarized next.

### *Similarity solutions*

An important step in terms of developing a physically based mixing model for salt fingers was made by Shen (1995), who performed two-dimensional simulations in a configuration compatible with the unbounded gradient model. Shen noticed that primary finger instabilities rapidly give way to more irregular patterns consisting of isolated "blobs," which move vertically and interact with each other (Fig. 3.3). These blobs are products of Holyer (1984) secondary instabilities of the vertical elevator modes. Shen suggested that the equilibration level is controlled by the dynamics of individual blobs, rather than by larger-scale collective instability waves, and developed a simple empirical theory for the equilibrium transport. His model assumed that (i) the size of blobs is comparable to the typical finger width, (ii) the vertical velocity of a blob can be estimated from the advective–diffusive balance, and (iii) the vertical transport is affected by the interactions between upward and downward propagating blobs. Shen's (1995) theory was found to be qualitatively consistent with simulations and observations. In particular, it predicted a rapid decrease of the vertical transport with the density ratio. This model
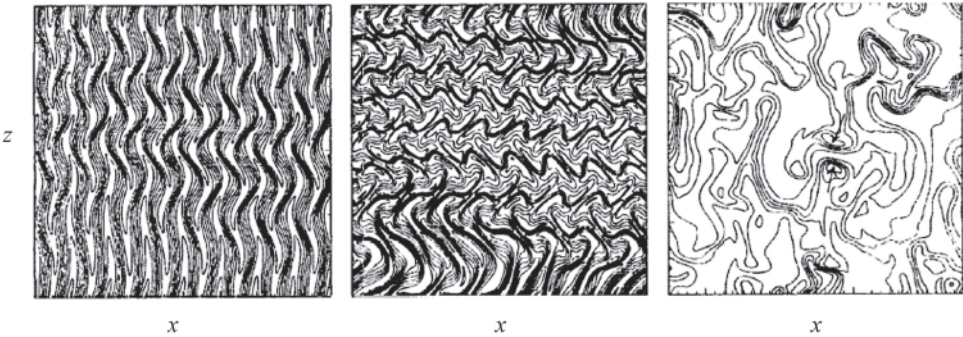
Figure 3.3 The simulated temperature field in fingering convection illustrating the flow evolution from incipient instability to disorganized convection. From Shen (1995).
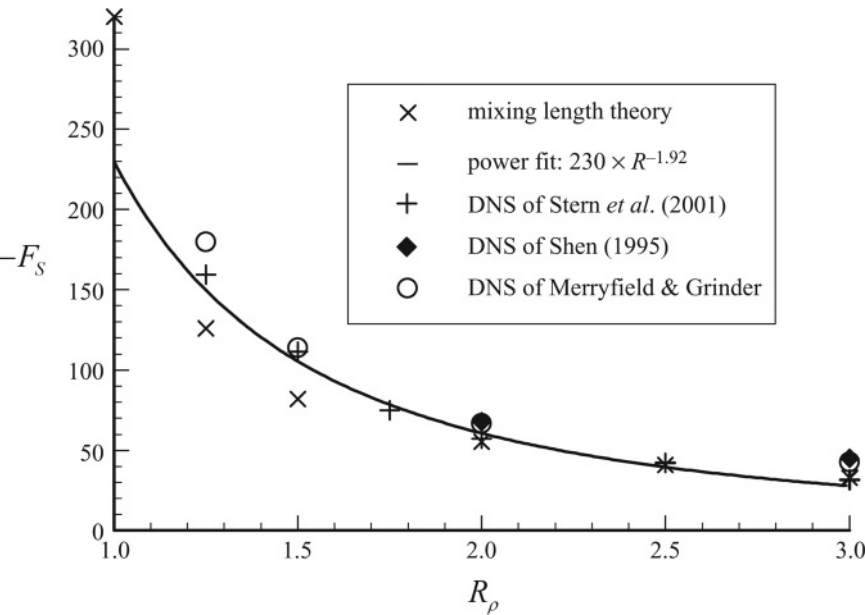


Figure 3.4 The non-dimensional salt flux as a function of the density ratio $R_\rho$. The prediction based on the mixing length theory is compared with the DNS results. From Stern and Simeonov (2005).

was refined and extended by Stern and Simeonov (2005), who suggested that the relevant vertical scale of temperature and salinity perturbations – the mixing length – is set by the size of the fastest growing Holyer instabilities. Figure 3.4 compares the flux prediction based on the mixing length theory with various numerical simulations in the unbounded configuration, revealing a reasonable agreement between all estimates.
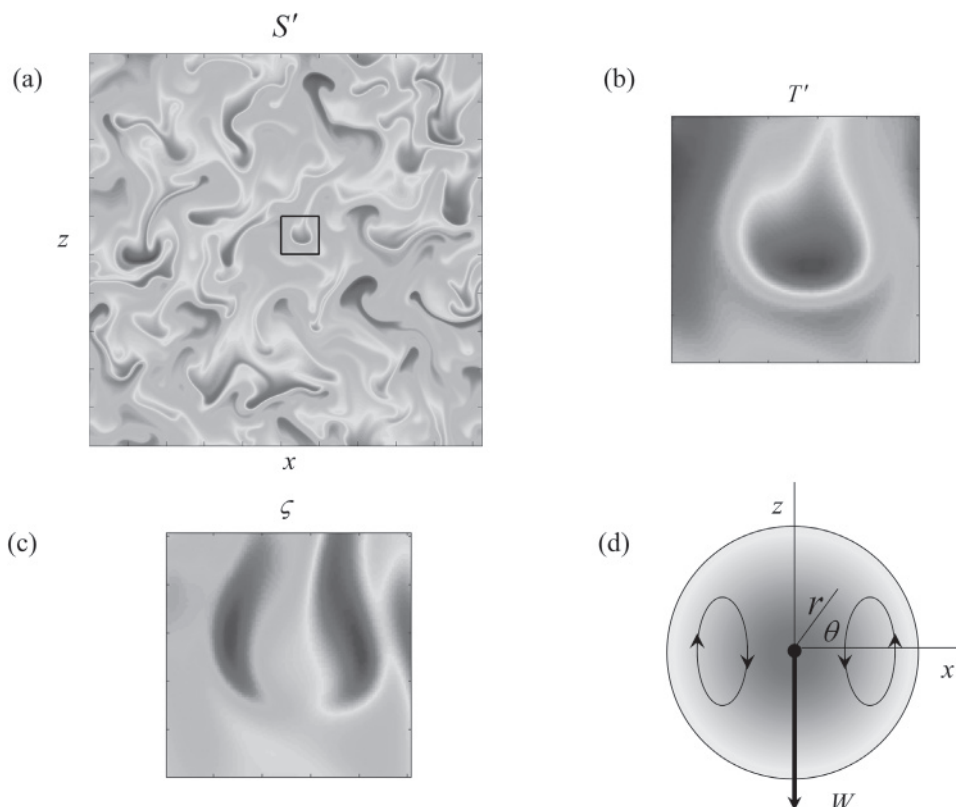
Figure 3.5 (a) Instantaneous salinity field in the numerical experiment with $R_\rho =$ 1.2, $Pr = 7$ and $\tau = \frac{1}{3}$. Red color corresponds to high values of $S'$ and low values are shown in blue. Distribution of temperature (b) and vorticity (c) in the square area marked in (a), which contains a well-defined double-diffusive modon. (d) Schematic diagram of the analytical similarity solution for the downward propagating modon. From Radko (2008). See color plates section.

    Radko (2008) attempted to explain the dynamics of coherent structures arising in double-diffusive convection by developing an explicit similarity solution for vertically propagating dipolar vortices − the double-diffusive modons. This nomenclature was adopted to emphasize the dipolar structure of the vorticity field and certain similarity to the "modon" solution proposed by Stern (1975) as a prototype of coherent oceanic vortices. Such structures are prevalent in the regime in which density stratification is close to neutral and fingering instability is extremely vigorous, as shown in the two-dimensional numerical experiment in Figure 3.5. Figure 3.5a presents the perturbation salinity pattern in the entire computational domain. The magnified images of one of the double-diffusive modons, looking particularly sweet and juicy, are shown in Figure 3.5b,c. Its temperature

pattern in Figure 3.5b indicates that the modon is roughly circularly symmetric; the temperature anomaly reaches maximum at the center and reduces to zero at the edge. The vorticity distribution in Figure 3.5c reveals the interior circulation pattern consisting of two symmetric, closely packed counter-rotating patches. The abundance of double-diffusive modons in numerical simulations motivated the search for corresponding analytical similarity solutions (see the schematic in Figure 3.5d). Such solutions – compact, dipolar and rectilinearly propagating – were obtained by expanding the governing equations in powers of the small parameter

$$\delta = \sqrt{1 - R_\rho^{-1}} \to 0, \tag{3.7}$$

and thus formally pertained only to the low density ratio regime. In this regard, the strongly nonlinear limit (3.7) is opposite to the large $R_\rho$ regime explored by the weakly nonlinear theory in Section 3.3.

The modon solution is the basis of a phenomenological mixing model in which salt-finger convection is represented by an array of vertically translating double-diffusive modons, as illustrated in the schematic diagram in Figure 3.6a. The leading-order balances of the governing equations for small $\delta$ suggest that each modon carries $T$–$S$ anomalies $T'$, $S' \propto \delta^{-\frac{1}{4}}$ and moves with speed $W \propto \delta^{-\frac{3}{4}}$. Hence, the vertical transport in the modon-flux model (Fig. 3.6a) should be proportional, at the leading order, to $\delta^{-1}$. The next term in the asymptotic expansion is of order one and the following terms are asymptotically small. Hence, for density ratios somewhat above unity, the vertical salt flux can be approximated by

$$- F_S \approx a \frac{1}{\sqrt{1 - R_\rho^{-1}}} + b, \tag{3.8}$$

where $a$ and $b$ are adjustable constants that can be determined by numerical experiments or field data. The prescription (3.8) was successfully tested by two-dimensional numerical simulations (Figs. 3.6b,c). Here, the variables are non-dimensionalized using the standard system (1.11) and the fluxes are plotted as a function of $R_\rho$. Note that the transport of heat and salt in fingering convection is downward and therefore the magnitude of fluxes is given by $(-F_T, -F_S) = (Nu, Nu/\gamma)$. The corresponding dimensional eddy diffusivities take the following form:

$$K_T \approx k_T \left( a \frac{1}{\sqrt{1 - R_\rho^{-1}}} + b \right), \quad K_s \approx \frac{R_\rho k_T}{\gamma} \left( a \frac{1}{\sqrt{1 - R_\rho^{-1}}} + b \right).$$

The applicability of this parameterization is yet to be examined in a broader context, including field measurements and simulations that are not necessarily limited to low density ratios (3.7).
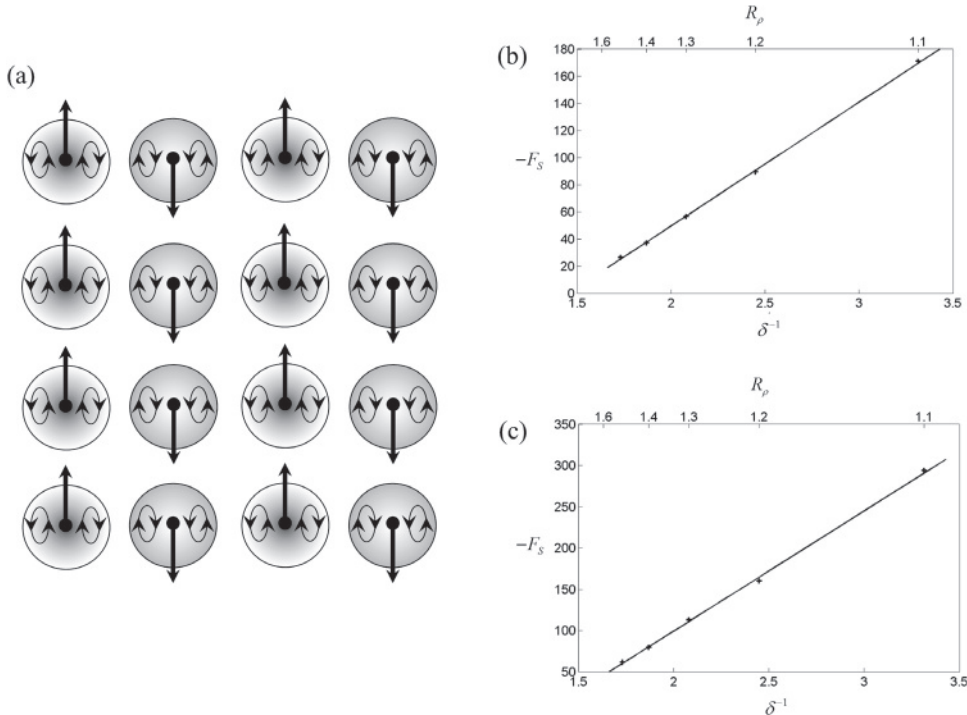
Figure 3.6 (a) Schematic illustration of the phenomenological mixing model that represents the fully developed fingering convection by a closely packed array of double-diffusive modons. The non-dimensional flux of salt ($F_S$) inferred from DNS is plotted as a function of $\delta^{-1} = \frac{1}{\sqrt{1 - R_\rho^{-1}}}$ for $\tau = 1/3$ (b) and $\tau = 1/12$ (c). Numerical data conform to the linear $F_S(\delta^{-1})$ relation suggested by the theory. From Radko (2008).

### *The growth rate balance*

In terms of the ability to represent the widest parameter range ($R_\rho$, $Pr$, $\tau$), perhaps the most general equilibrium model to date has been proposed by Radko and Smith (2012). These authors based their theory on the "growth rate balance." As weak, initially linear, salt fingers grow, they develop secondary instabilities (Fig. 3.1). Radko and Smith hypothesized that the equilibration of salt fingers occurs when the growth rates of primary ($\lambda_1$) and secondary ($\lambda_2$) instabilities become comparable:

$$\lambda_2 = C\lambda_1. \tag{3.9}$$

The coefficient $C$ in (3.9) is a dimensionless order-one constant that can be calibrated on the basis of simulations or experiments. The primary growth rate is determined by the background gradients of temperature and salinity, as well as

by molecular characteristics (diffusivities and viscosity). The secondary instability is also affected by these quantities, but, additionally, it depends very strongly on the amplitude of primary salt fingers. Thus, for any given background state and value of $C$, the growth rate balance (3.9) implicitly determines the equilibrium amplitude of salt fingers. The physical reasoning behind the growth rate balance is straightforward. When salt fingers start to emerge from random small-scale perturbations, their secondary instabilities are too weak to significantly perturb primary modes – the evolution of small-amplitude fingers is captured by the linear theory. However, as the amplitude of fingers increases, the growth rate of secondary instabilities significantly exceeds the primary growth rates. As a result, the secondary instabilities start to gain in magnitude, rapidly reaching the level of primary modes. When the amplitude of secondary instability is large enough, it nonlinearly suppresses the growth of salt fingers. At this stage, the system reaches statistical equilibrium.

This scenario is supported by the numerical simulation in Figure 3.7, which shows the typical evolution of salt fingers from small-amplitude random noise to statistically steady convection. During the initial stage of linear growth ($t = 20$ in Fig. 3.7a) the flow field is dominated by vertically uniform salt fingers. This pattern is consistent with the linear stability theory, which predicts that the most rapidly growing perturbations take the form of vertical elevator modes. Figure 3.7b presents the temperature field in the fully developed equilibrium regime ($t = 50$). While the previously dominant elevator mode is still visible, it is now comparable in magnitude to the irregular transient structures produced by secondary instabilities, which act to distort the vertical fingers, adversely affecting their growth. The rapid transition in the flow pattern is reflected in the heat and salt flux records (Fig. 3.7c). As previously, the standard system of non-dimensionalization (1.11) is used. The initial stage of the simulation is characterized by the exponential growth of fluxes, which is followed by their equilibration at $t \sim 30$. After equilibration, the intensity of salt fingering remains statistically steady.

Figure 3.8 presents the heat flux (a), salt flux (b) and the flux ratio (c) as functions of the density ratio, evaluated from the growth rate balance theory (3.9) for $C = 2.7$. The theoretical predictions (solid curves) are plotted along with the corresponding DNS results (plus signs) and with the explicit empirical fit to the numerical data (dashed curves):

$$\begin{cases} -F_S = \dfrac{a_S}{\sqrt{R_\rho - 1}} + b_S, & (a_S, b_S) = (135.7, -62.75), \\ \gamma = a_\gamma \exp(-b_\gamma R_\rho) + c_\gamma, & (a_\gamma, b_\gamma, c_\gamma) = (2.709, 2.513, 0.5128), \\ F_T = \gamma F_S. \end{cases} \quad (3.10)$$

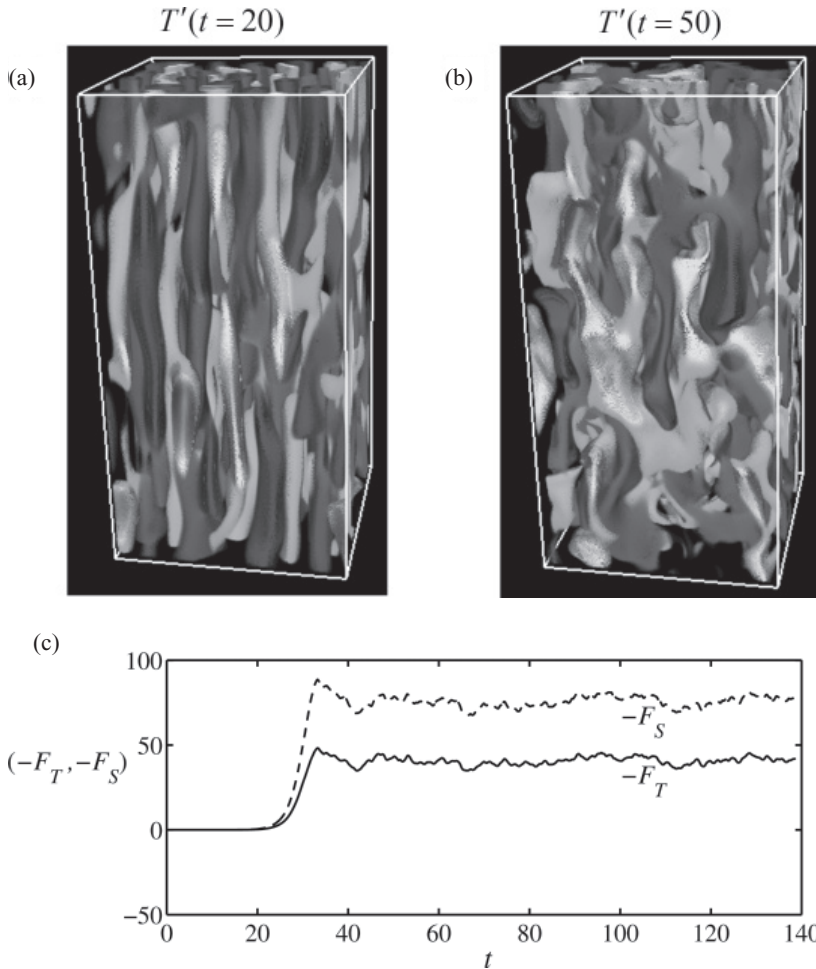$$T'(t = 20) \qquad\qquad T'(t = 50)$$



Figure 3.7 Equilibration of salt fingers in the numerical experiment with $Pr = 7$, $\tau = 0.01$ and $R_\rho = 1.9$. The temperature fields are shown for (a) the early stage of linear growth at $t = 20$ and (b) the fully equilibrated state at $t = 50$. Red/green corresponds to high values of $T$ and low values are shown in blue. (c) Time record of the temperature (solid curve) and salinity (dashed curve) fluxes. From Radko and Smith (2012). See color plates section.

In addition to the heat–salt case, Radko and Smith (2012) examined other combinations of the governing parameters, varying $Pr$ by four orders of magnitude and $\tau$ by a factor of thirty. In each regime, the growth rate balance theory adequately describes the (rapidly decreasing) dependence of fluxes on density ratio. The calibrated coefficients $C$ are fairly stable. In all cases, the values of $C$ are limited to a relatively narrow range $1.6 < C < 2.7$. The theoretical prediction with $C = 2$ in (3.9) explains all the numerical fluxes to within a factor of two.
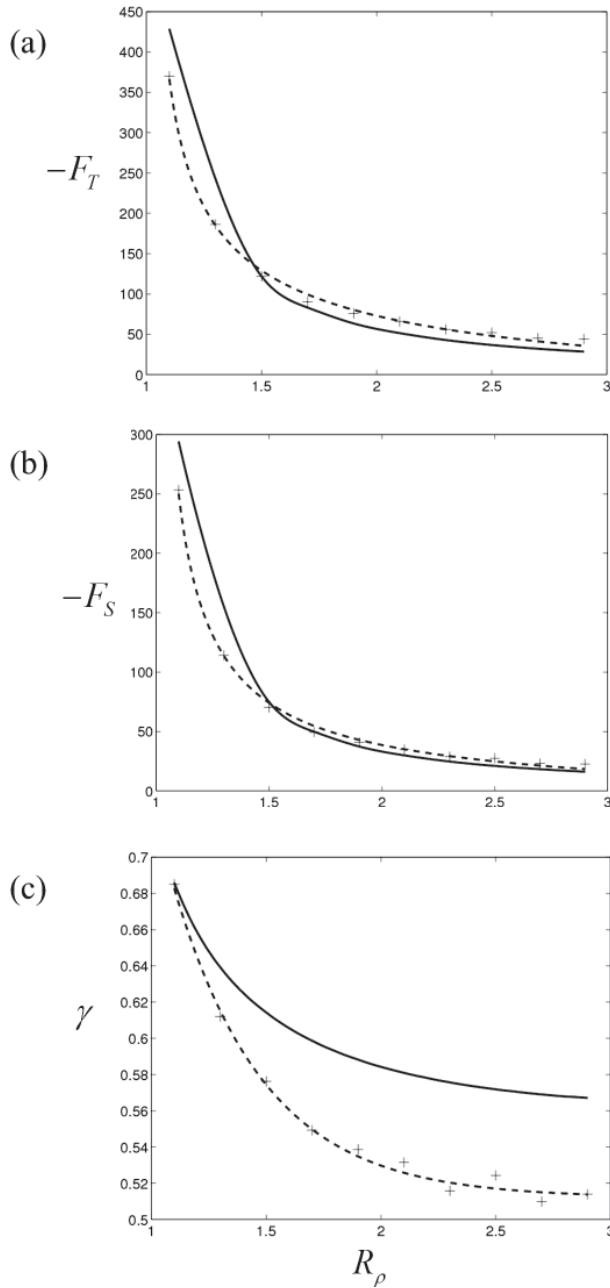
Figure 3.8 Comparison of the theoretical growth rate balance model for $C = 2.7$ (solid curve) with DNS (plus signs). The heat flux, salt flux and flux ratio are shown in (a), (b) and (c) respectively. The dashed curves represent the empirical expressions (3.10). From Radko and Smith (2012).

### *Empirical parameterizations*

An important role in the double-diffusive literature is played by various ad hoc parameterizations, which are based entirely on external observational (Schmitt, 1981; Zhang *et al*., 1998) or numerical data (Stern *et al*., 2001; Stern and Simeonov, 2004; Kimura *et al*., 2011). While such parameterizations do not address the physical principles of equilibration, they serve an important practical purpose – representing salt fingers in large-scale numerical and theoretical models. The simplicity of the proposed expressions for eddy diffusivities becomes an important consideration in the formulation of such parameterizations. Table 3.1 presents a list of various parameterizations that have been used in double-diffusive studies. It is encouraging to see qualitative agreement between various models in terms of predicting the rapid decrease of the heat and salt diffusivities with increasing density ratio. The mismatch in the diffusivity values is generally limited to a factor of two to three. It is also worth noting that even the earliest model (Schmitt, 1981) − essentially an educated guess of the flux law − adequately captures the pattern of heat–salt diffusivities inferred from recent simulations and observations.

Promising attempts have also been made (Canuto *et al*., 2002, 2008) to extend the second-order closure models, commonly used in turbulence research, to incorporate double-diffusive mixing. Such models use governing equations to relate the second-order moments of dynamic variables. Since these relations are generally insufficient to close the problem, additional assumptions are made to bring the resulting solutions into agreement with the available data. Therefore, a certain degree of empiricism involved in the development of such models seems to be inevitable.

## 3.5  Numerical simulations

The classic masterpiece *Anna Karenina* by Leo Tolstoy starts with an observation, "All happy families resemble one another, each unhappy family is unhappy in its own way." If this principle were extended to modeling communities, we would have to conclude that groups of double-diffusers are truly happy as their efforts and products are mutually consistent and often resemble each other.

The most natural and common numerical configuration used to represent the unbounded model assumes periodic, in all spatial dimensions, boundary conditions for temperature, salinity and velocity perturbations of the uniform background gradients. Two-dimensional DNS of this type were performed by Whitfield *et al*. (1989), Shen (1995), Stern and Radko (1998), Merryfield (2000), Merryfield and Grinder (2002), Stern and Simeonov (2002,

Table 3.1 *Various double-diffusive parameterizations of salt diffusivity and flux ratio as a function of density ratio*

| Model, type | Salt diffusivity ($K_S$) | Flux ratio ($\gamma$) | Coefficients | Basis |
|---|---|---|---|---|
| Schmitt (1981), SF | $\dfrac{K_0}{1+\left(\frac{R_\rho}{R_c}\right)^n}+K_\infty$ | 0.7 | $K_0 = 10^{-3}\,\text{m}^2\,\text{s}^{-1}$ $K_\infty = 5 \cdot 10^{-6}\,\text{m}^2\,\text{s}^{-1}$ $R_c = 1.7$ $n = 32$ | Obs. |
| Merryfield *et al.* (1999), SF Zhang *et al.* (1998), SF | $\dfrac{K_0}{1+\left(\frac{R_\rho}{R_c}\right)^n}+K_\infty$ | 0.7 | $K_0 = 10^{-2}\,\text{m}^2\,\text{s}^{-1}$ $K_\infty = 3 \cdot 10^{-5}\,\text{m}^2\,\text{s}^{-1}$ $R_c = 1.6$ $n = 6$ | Obs. |
| Large *et al.* (1994), SF | $K_f\left[1-\left(\dfrac{R_\rho - 1}{R_\rho^0 - 1}\right)^2\right]^p,$ $1 < R_\rho < R_\rho^0$ $0,\ R_\rho < R_\rho^0$ | 0.7 | $K_f = 10^{-3}\,\text{m}^2\,\text{s}^{-1}$ $R_\rho^0 = 1.9$ $p = 3$ | Obs. |
| Merryfield and Grinder (2002), SF | $0.15\dfrac{1-\tau R_\rho}{R_\rho - \gamma}$ | 0.6 | | DNS |
| Simeonov and Stern (2004), SF | $\dfrac{158}{\gamma R^2}k_T$ | 0.62 | | DNS |
| Kimura *et al.* (2011), SF | $4.38 \cdot 10^{-5} R_\rho^{-2.7} Ri^{0.17}$ | $0.7 R_\rho^{-0.3}$ | | DNS |
| Radko and Smith (2012), SF | $\left(\dfrac{a_S}{\sqrt{R_\rho - 1}} + b_S\right)k_T R_\rho$ | $a_\gamma \exp(-b_\gamma R_\rho) + c_\gamma$ | $(a_S, b_S) = (135, -62.75)$ $(a_\gamma, b_\gamma, c_\gamma) = (2.709,$ $2.513, 0.5128)$ | DNS |
| Fedorov (1988), DC | $0.909\nu\dfrac{\gamma^*}{R_\rho^*}$ $\times \exp\left(4.6\exp[-0.54(R_\rho^* - 1)]\right)$ | $\gamma^* = 1.85 - 0.85 R_\rho^*,\ 1 < R_\rho^* < 2$ $\gamma^* = 0.15,\ R_\rho^* > 2$ | | Obs., Expts. |
| Kelley (1984, 1990), DC | $\gamma^* C R_a^{1/3} k_T$ | $\gamma^* = \dfrac{R_\rho^* + 1.4(R_\rho^* - 1)^{3/2}}{1 + 14(R_\rho^* - 1)^{3/2}}$ | $C = 0.0032\exp\left[4.8(R_\rho^*)^{-0.72}\right]$ $R_a = 0.25 \cdot 10^9 R_\rho^{1.1}$ | Obs., Expts. |

Salt-finger models are denoted by SF and diffusive models as DC.

The parameterizations are based on observations (Obs.), direct numerical simulations (DNS) and laboratory experiments (Expts.).

2005), Radko (2008, 2010) and Denissenkov (2010). Three-dimensional DNS are more challenging computationally but nevertheless are becoming increasingly common (Radko and Stern, 1999; Stern *et al.*, 2001; Denissenkov and Merryfield, 2011; Stellmach *et al.*, 2011; Traxler *et al.*, 2011a; Mirouh *et al.*, 2012; Radko and Smith, 2012). The unbounded configuration is ideally suited for the use of spectral methods based on Fourier basis functions (Canuto *et al.*, 1987), and such models have dominated the DNS of double-diffusion. With minor modifications, spectral models can be applied to studies of double-diffusion in external shear (Smyth and Kimura, 2007; Kimura and Smyth, 2011). The latter studies will be discussed in greater detail in Chapter 10.

A particularly encouraging aspect of fingering simulations is related to the pronounced lack of sensitivity to details of the numerical setup. The size and aspect ratio of the computational domain have very limited effects on the intensity and patterns of double-diffusion as long as the box size significantly exceeds the typical salt-finger scale. Radko and Stern (1999), for instance, observed that an increase in the height of the salt-finger zone by a factor of ten changes the vertical *T–S* transport by only a small percentage. Boundary conditions also do not affect the major characteristics of salt fingering. Calculations in which the salt-finger zone is sandwiched between relatively homogeneous reservoirs (i.e., Kimura *et al.*, 2011) produce vertical diffusivities consistent with models assuming uniform background stratification (Stern *et al.*, 2001; Traxler *et al.*, 2011a). We note in passing that the robust, modeler-friendly nature of double-diffusion is in great contrast with the properties of thermal convection in a triply periodic system – the so-called homogeneous Rayleigh–Bénard problem (Borue and Orszag, 1996; Calzavarini *et al.*, 2006). In homogeneous thermal convection, the fastest growing modes span the entire domain and depend sensitively on the aspect ratio of the computational box, as well as on other numerical details. The typical length scale of eddies in the fingering regime is set by the diffusive length scales and is independent of the box size, which accounts for the dramatic difference between the two problems.

The generic difficulty in performing numerical simulations of double-diffusive convection is related to the necessity to resolve a wide range of scales. The smallest dynamically significant scale is that of salt dissipation ($d_S$); the scale of heat dissipation ($d_T$) is larger by factor of $\tau^{-1/2}$. The heat dissipation scale, in turn, is less than the finger scale ($L$) by a factor of $Nu^{-1/4}$. Problems in addressing the interplay between salt fingers and waves, shear, convective cells or intrusions necessarily require resolving even larger scales of motion. But even if we temporarily exclude such problems from consideration, the challenge is still formidable. For typical oceanographic conditions ($\tau \sim 0.01$, $Nu \sim 100$) the scale of salt dissipation is about thirty times smaller than the salt-finger width. Thus, a simulation representing

several fingers requires computational grids on the order of $1000^3$. Simulations of this order have only recently become possible (Traxler *et al*., 2011a; Stellmach *et al*., 2011). Earlier three-dimensional simulations either used a diffusivity ratio that is substantially higher than the heat–salt value or failed to resolve the salt-dissipation scale.

However, to be fair to the early studies, it should be mentioned that none of these shortcomings resulted in major quantitative errors. As discussed in Stern *et al*. (2001) and Radko (2008), use of a moderate diffusivity ratio is not expected to alter the fundamental physics and characteristics of salt fingering, as long as $\tau$ remains significantly less than unity. For instance, the four-fold decrease in the diffusivity ratio, from $\tau = 1/12$ to $\tau = 1/48$, results in about a 15% increase in vertical *T–S* transport. Traxler *et al*. (2011a) note that the impact of resolution is even less. Their computational domain, equivalent in size to $5 \times 5 \times 10$ finger widths, was discretized on a $768 \times 768 \times 1536$ grid, which was barely sufficient to resolve the salt-dissipation scale. Remarkably, the much coarser resolution of $96^3$ yields fluxes that are within 20% of their fully resolved counterparts. The lack of sensitivity to the precise values of $\tau$ and to the resolution of the salinity scale suggests that salt dissipation plays a rather passive role in fingering dynamics. The mixing intensity is apparently controlled by processes operating on the much larger finger scales ($L$) and this suggestion is supported by most theoretical models of salt fingers (Sections 3.3 and 3.4). With regard to resolution issues, the modeling of double-diffusion once again proves to be a much more rewarding task than the modeling of homogeneous thermal convection, which is highly sensitive to numerical truncations (Borue and Orszag, 1996; Calzavarini *et al*., 2006).

To be specific in describing double-diffusive simulations, consider a representative treatment of the unbounded model in the recent numerical study by Traxler *et al*. (2011a). Figure 3.9 presents typical salinity patterns in the fully developed fingering flow. The high density ratio simulations (e.g., Fig. 3.9d) result in relatively laminar vertically elongated fingers. However, as $R_\rho$ decreases, the flow rapidly becomes more disorganized and isotropic (Fig. 3.9b,c). The heat and salt fluxes, non-dimensionalized using (1.11), rapidly decrease with $R_\rho$ (Fig. 3.10a,b) and are consistently higher in three dimensions than in two dimensions. The pattern of the flux ratio (Fig. 3.10c) is generally consistent with the prediction of linear theory (Section 2.3) although some quantitative differences are visible. For instance, linear theory consistently overestimates values of $\gamma(R_\rho)$ and its minimum is shifted towards higher $R_\rho$ in DNS. The two-dimensional DNS are closer to the theoretical prediction than the three-dimensional ones. Finally, the Stern number (Fig. 3.10d) rapidly decreases with density ratio. The values of eddy diffusivities and of other integral characteristics for each $R_\rho$ are listed in Table 3.2.
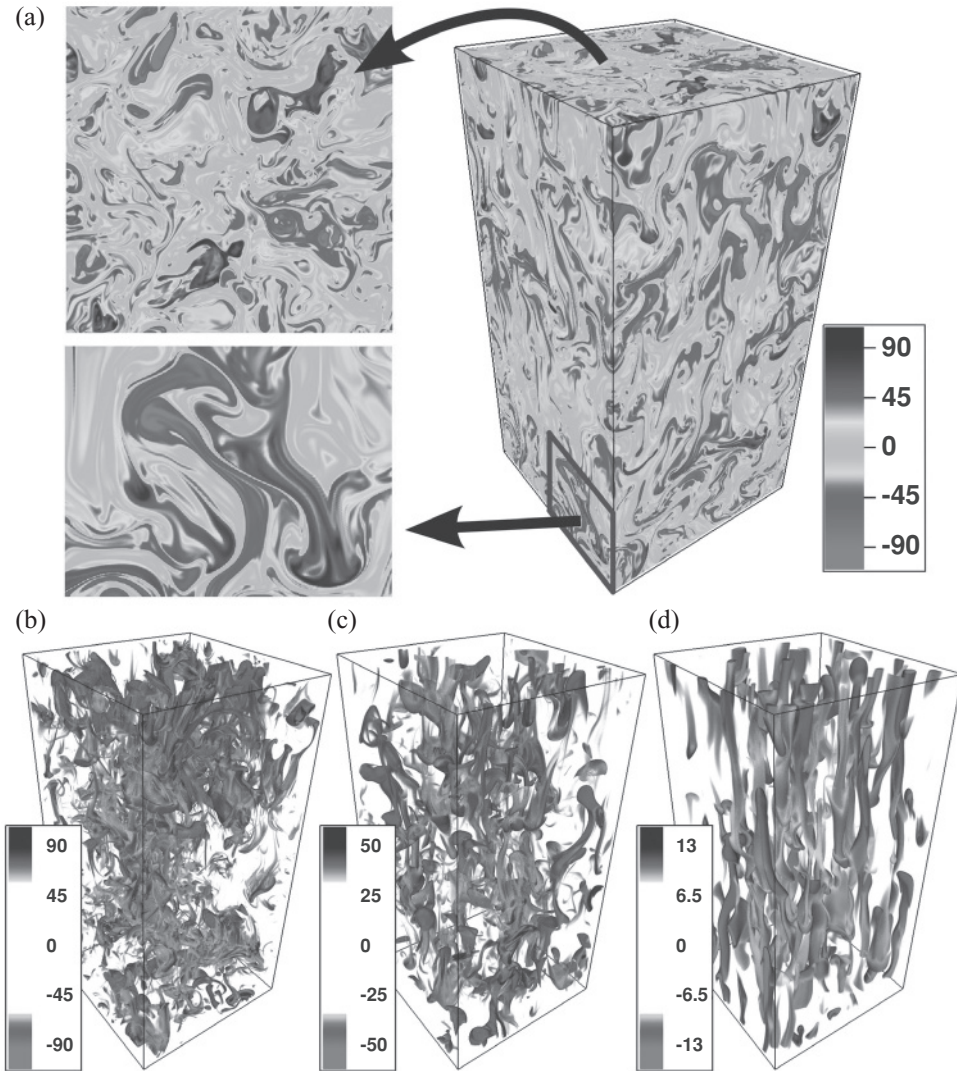
Figure 3.9 Snapshots of the salinity field in simulations of fingering convection for $Pr = 7$, $\tau = 0.01$. (a) Salinity field at $R_\rho = 1.2$, plotted on the three planes of the computational domain. (b)–(d) Volume rendering of the salinity field for $R_\rho = 1.2$, $R_\rho = 2$ and $R_\rho = 10$ (from left to right). From Traxler *et al.* (2011a). See color plates section.

## 3.6 Laboratory experiments

Modeling the effectively unbounded system in the laboratory requires creating a relatively thick gradient region, where fingers are vertically correlated over a fraction of the entire domain. There are at least two methods for creating such deep gradient regions.
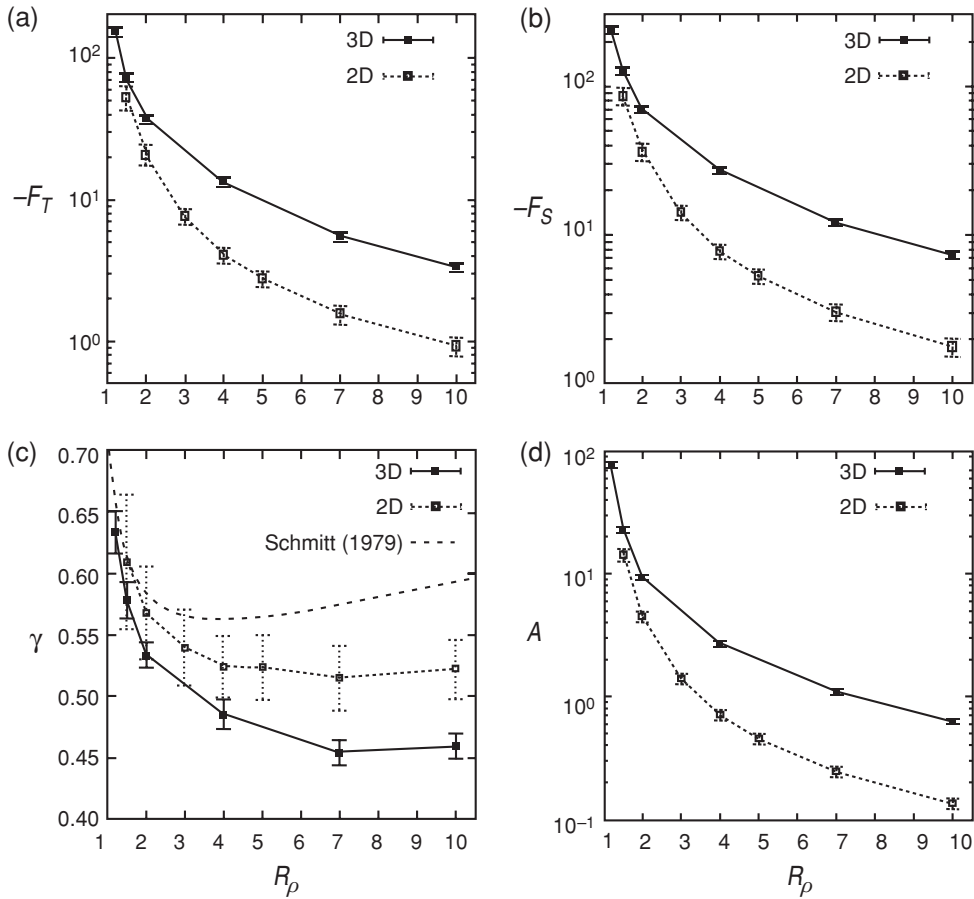
Figure 3.10 Parametric dependence of the non-dimensional fluxes $F_T$ and $F_S$ as well as their ratio $\gamma$ and of the Stern number $A$ as a function of $R_\rho$. Results from both three- and two-dimensional simulations are shown. Panel (c) also contains a theoretical prediction of $\gamma(R_\rho)$ based on the fastest growing linear model (Schmitt, 1979a). From Traxler *et al.* (2011a).

For two-solute experiments, such as the sugar–salt system (Stern and Turner, 1969; Linden, 1978; Krishnamurti, 2003), a deep double gradient can be created using the "double-bucket" technique, which is illustrated in Figure 3.11. A pure *T*-solution (e.g., salt) in one bucket is connected by a siphon to a second bucket at the same elevation containing a pure *S*-solution (e.g., sugar) of lesser density. The latter is connected by another siphon to the bottom of the experimental tank located at a lower level. When both siphons are opened, *S*-fluid enters the tank, and *T*-fluid flows into the *S*-bucket where it is completely mixed by a mechanical stirrer. The diluted mixture then enters the tank bottom underneath the slightly

Table 3.2 *Summary of fingering heat–salt simulations in a computational domain containing 5 × 5 × 10 fastest growing finger wavelengths*

| | $R_\rho = 1.2$ | $R_\rho = 1.5$ | $R_\rho = 2.0$ | $R_\rho = 4$ | $R_\rho = 7$ | $R_\rho = 10$ |
|---|---|---|---|---|---|---|
| Resolution | $768^2 \times 153^6$ | $768^2 \times 1536$ | $384^2 \times 768$ | $384^2 \times 768$ | $384^2 \times 768$ | $384^2 \times 768$ |
| $t_{average}$ | 39.1 | 57.8 | 121.2 | 223.8 | 422.7 | 390.1 |
| $|F_T|$ | $153.5 \pm 11.7$ | $73.2 \pm 5.7$ | $37.6 \pm 2.2$ | $13.3 \pm 1.0$ | $5.48 \pm 0.38$ | $3.35 \pm 0.21$ |
| $|F_S|$ | $241.8 \pm 13.1$ | $126.4 \pm 7.5$ | $70.3 \pm 3.1$ | $27.4 \pm 1.5$ | $12.1 \pm 0.65$ | $7.29 \pm 0.34$ |
| $\gamma$ | $0.63 \pm 0.02$ | $0.58 \pm 0.01$ | $0.53 \pm 0.01$ | $0.49 \pm 0.01$ | $0.45 \pm 0.01$ | $0.46 \pm 0.01$ |
| $\sqrt{\langle u^2 \rangle}$ | $14.1 \pm 0.4$ | $9.4 \pm 0.3$ | $6.5 \pm 0.15$ | $3.7 \pm 0.1$ | $2.37 \pm 0.06$ | $1.82 \pm 0.04$ |
| $K_T$ [$10^{-6}$ m$^2$ s$^{-1}$] | $21 \pm 2$ | $10 \pm 1$ | $5.3 \pm 0.3$ | $1.9 \pm 0.1$ | $0.77 \pm 0.05$ | $0.47 \pm 0.03$ |
| $K_S$ [$10^{-6}$ m$^2$ s$^{-1}$] | $41 \pm 2$ | $27 \pm 2$ | $20 \pm 1$ | $15 \pm 1$ | $11 \pm 1$ | $10 \pm 0.5$ |
| $A$ | $76 \pm 3$ | $23 \pm 1$ | $9.4 \pm 0.3$ | $2.7 \pm 0.1$ | $1.1 \pm 0.05$ | $0.63 \pm 0.03$ |

$t_{average}$ denotes the length of the time interval over which the data have been averaged.
The non-dimensionalization is based on the standard double-diffusive transformation in (1.11).
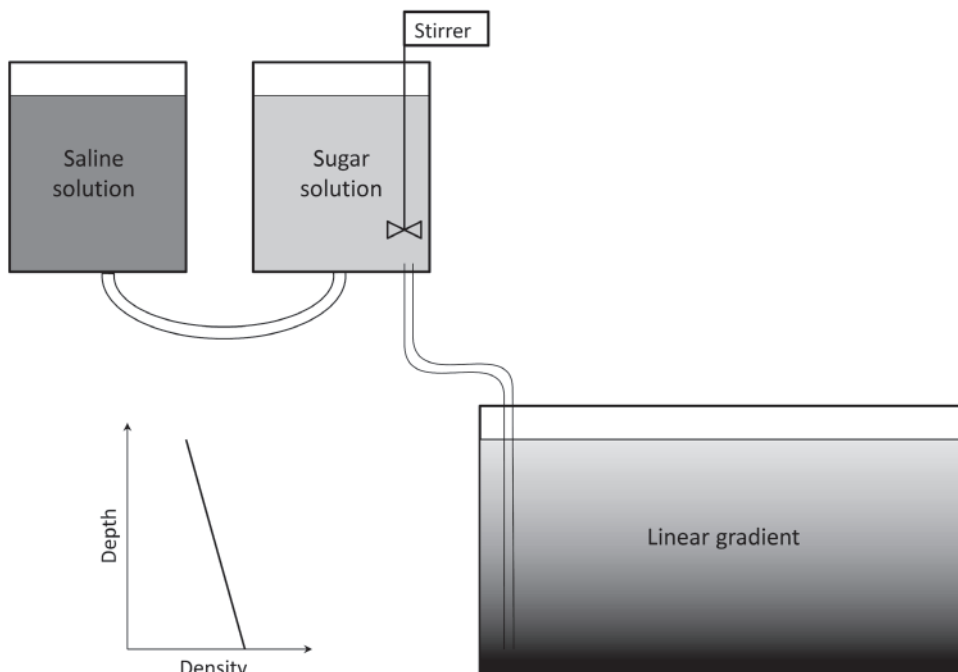From Traxler *et al*. (2011a).

Figure 3.11 Schematic diagram of the double-bucket method for creating extended vertical property gradients in laboratory experiments.

lighter *S*-fluid, until the tank is filled with pure *S*-fluid (sugar) at the top, pure *T*-fluid (salt) at the bottom, and with nearly uniform *T*–*S* gradients in-between. For suitable filling conditions and moderately large density ratio, the up-going and down-going salt fingers form and occupy the entire tank (Stern and Turner, 1969). The double-bucket technique has been conveniently used in experimental studies of the interaction between salt fingers and shear (Wells *et al*., 2001), interaction with intermittent turbulence (Wells and Griffiths, 2003) and effects of localized stirring (Wells and Griffiths, 2002) – topics that will be discussed in greater detail in Chapter 10. If the vertical gradients are not maintained continuously, the system runs down and the background density ratio systematically drifts towards larger and larger values. In many cases, it is possible to take advantage of the inherent time dependence in the run-down experiments. For instance, a single experiment of this type yields a continuous record of salt-finger characteristics as a function of the density ratio.

However, time dependence can occasionally lead to unintended adverse consequences. For instance, the formation and evolution of thermohaline staircases (Krishnamurti, 2003, 2009) and intrusions (Krishnamurti, 2006) occur on temporal scales that greatly exceed the finger scales. Thus, in order to realistically
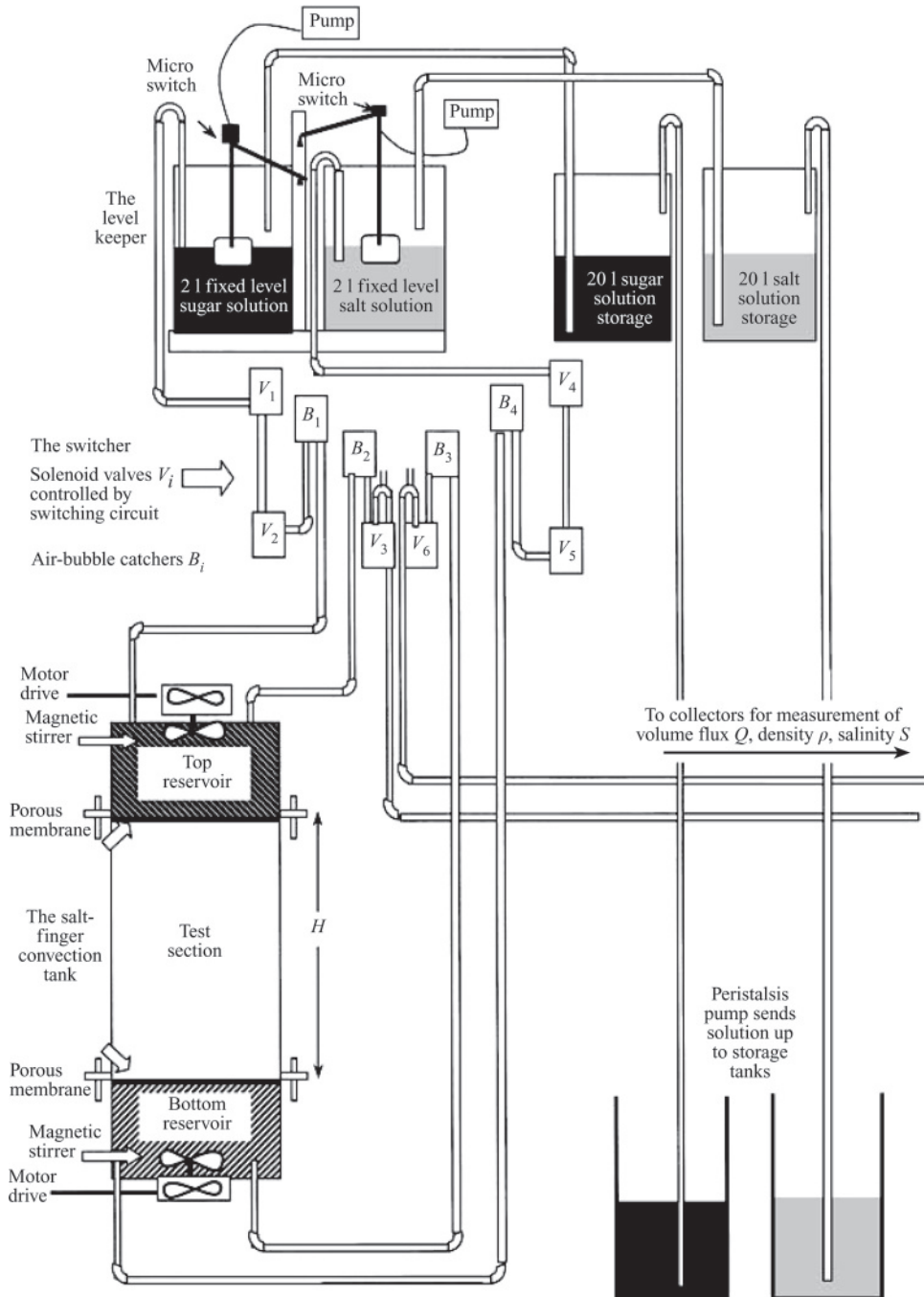
Figure 3.12 Schematic diagram of the apparatus designed to maintain the background stratification during fingering experiments. From Krishnamurti (2003).
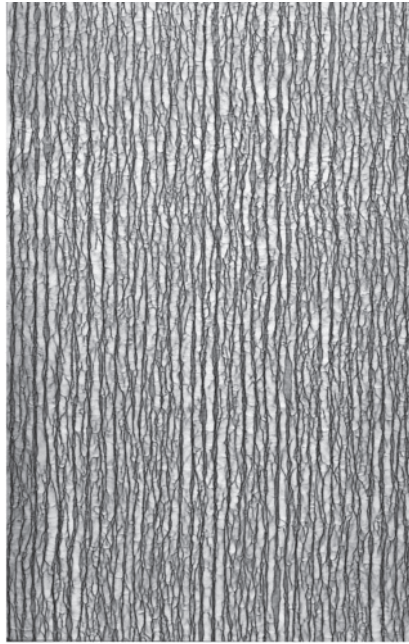
Figure 3.13 Shadowgraph of sugar–salt fingers for $R_\rho = 1.25$. Shown here is an excerpt from a 2 m tall shadowgraph. The width of the image corresponds to 8.5 cm. From Krishnamurti (2003).
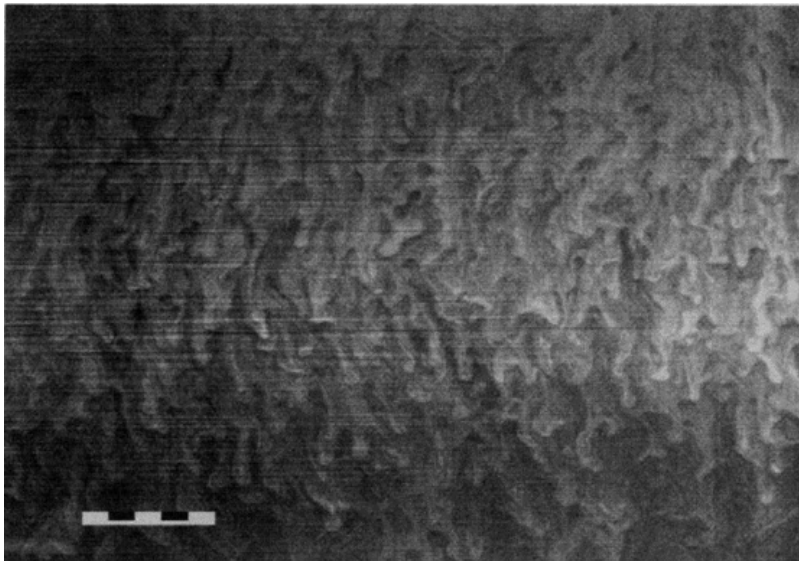


Figure 3.14 Salt fingers forming in the extended vertical gradient created by displacing a metal grid across the interface between two initially homogeneous layers. The scale bar is 5 cm long. From Taylor (1993).

represent these slow secondary double-diffusive structures and to quantify their control by the background *T–S* gradients, it is imperative to maintain the vertical stratification in the course of an experiment. Such fixed-gradient experiments are more involved technically. The schematic in Figure 3.12 illustrates the experimental setup designed and used by Krishnamurti (2003). Initially, the "test section" is filled with linear salt-finger favorable gradients using the double-bucket method. The working fluid is bounded by two reservoirs of specified salinity and temperature, which are separated from the test section by rigid porous membranes. To maintain constant in time *T–S* values in the reservoirs, they are periodically flushed. This procedure is equivalent to enforcing the prescribed vertical boundary conditions for the gradient region in the test section. In this manner, the background interior stratification is sustained throughout the duration of an experiment, which can easily last for weeks. A shadowgraph of a thick gradient sugar–salt experiment is shown in Figure 3.13 (Krishnamurti, 2003), revealing vertically elongated fingers, typical of the large *Pr*/moderate $R_\rho$ regime.

For heat–salt experiments, the double-bucket method may not be as effective as in two-solute systems because of the inevitable heat loss to the environment. An alternative method for creating extended gradient layers was proposed by Taylor (1991, 1993). Initially, a two-layer heat–salt system is created and then the interface between homogeneous layers is mechanically thickened by vertically displacing a metal grid. The result is a deep double-gradient such as shown in Figure 3.14. Taylor (1993) used this technique to study the anisotropy of salt fingers in the gradient layers. One of the conclusions from these experiments is that at relatively low density ratios $1 < R_\rho < 3$, relevant for much of the mid-latitude thermocline, salt fingers take the form of relatively isotropic blobs, whereas the increase in $R_\rho$ makes fingers progressively more elongated. The link between the density ratio and the anisotropy of salt fingers is robust and readily reproducible by DNS (e.g., Fig. 3.9).